Magnetically controllable nonreciprocal Goos-Hänchen shift supported by a magnetic plasmonic gradient metasurface

Huabing Wu,[1] Qilin Luo,[2] Huajin Chen,[3,4] Ying Han,[4] Xinning Yu,[4] and Shiyang Liu[1,4,*]

[1]*Institute of Information Optics, Zhejiang Normal University, Jinhua, Zhejiang 321004, China*

[2]*School of Physical Science and Technology, Yulin Normal University, Yulin, Guangxi 537000, China*

[3]*School of Electrical and Information Engineering, Guangxi University of Science and Technology, Liuzhou, Guangxi 545006, China*

[4]*Department of Physics, State Key Laboratory of Surface Physics, Fudan University, Shanghai 200433, China*

(Received 14 November 2018; published 11 March 2019)

We demonstrate a magnetically controllable nonreciprocal Goos-Hänchen (GH) shift enabled by the magnetic plasmonic gradient metasurfaces (GMSs) consisting of an array of ferrite rods with a rotation gradient introduced to the rod dimers in the unit cell. The incident Gaussian beam is observed to exhibit an evident GH shift about 5λ when it is incident from one side, whereas for the Gaussian beam incident from the geometrically symmetric direction with respect to surface normal only a very small GH shift comes into appearance. The phenomenon arises from the unidirectional coupling of the incident beam with the magnetic plasmonic GMSs due to the time-reversal-symmetry-breaking nature of the magnetic system as evidenced from the photonic band diagrams of the edge states. The unidirectional GH shift can also be implemented at different incident angles by either engineering the gradient of the GMSs or tuning the bias magnetic field. By designing the magnetic plasmonic GMSs with more exquisite configurations we can expect a lot more nonreciprocal properties, adding additional freedom in manipulating electromagnetic waves.

DOI: 10.1103/PhysRevA.99.033820

I. INTRODUCTION

As is well known, the reflection of a plane wave at the interface between two homogenous media can be determined straightforwardly from geometric optics, whereas for a bounded light beam with finite transverse extent the totally reflected light beam will be shifted at the interface either along the longitudinal direction on the incident plane, termed the Goos-Hänchen (GH) shift [1] or along the transverse direction normal to the incident plane, termed the Imbert-Fedorov (IF) shift [2–4]. Physically, these lateral shifts arise from diffractive correction due to the different reflection phase changes of each plane-wave component of a light beam [5,6]. Theoretically, these lateral shifts can be clearly interpreted by the stationary phase theory [7] and the energy flux method [8] for the interfaces between homogeneous media involving dielectrics [9,10], metals [11,12], nonlinear materials [13,14], and graphene-related systems [15,16]. In a recent decade, the phenomenon still captured intensive attractions owing to the emergence of structured electromagnetic media, such as photonic crystals and metamaterials, together with the potential promising applications in optical switching and sensing [10,17,18]. Photonic crystals can mold the electromagnetic properties by engineering the photonic dispersion curves so that the Bloch surface wave can be excited and the phase of the complex reflection coefficient can be tuned, rendering more degrees of freedom to manipulate the GH and IF shifts [19,20]. Metamaterials, in principle, can implement arbitrary permittivity and permeability by creating artificial electric and magnetic responses, which provide new platforms to examine the performance of the GH and IF shifts in the systems not found in nature, typically, zero index materials [21,22], negative index materials [5,23], hyperbolic materials [24], and even custom-made transformation media [25]. Due to its universality, the phenomenon was also observed in other physics fields including acoustics [26], neutron physics [27], especially, spintronics [28,29], and quantum mechanics [30,31].

Metasurfaces are a kind of two-dimensional planar metamaterials [32,33], which enable the simultaneous control over the amplitude, phase, and even polarization of the photon by rectifying its interaction with gradient metasurfaces (GMSs), giving rise to a variety of novel functionalities with high performance. Compared to the photonic crystals and metamaterials, GMSs exhibit superior properties, such as low cost, low loss, easy fabrication, and, most importantly, integration compatibility for photonics and electronics [32]. Quite many striking physical phenomena ranging from wavefront shaping [34,35] and anomalous reflection and refraction [36,37] to polarization conversion [38,39] and photonic spin Hall effect [40,41] were implemented theoretically and experimentally, resulting in a great deal of promising applications from ultrathin wave plates [42,43] and metalens [44,45] to hologram design [46,47] and dynamic color display [48,49]. In addition, GMSs can also be employed to excite and guide a surface wave and, furthermore, realize the phase control [50,51], which is closely related to the GH and IF shifts. As a result, GMSs can be served to manipulate these lateral shifts, whereas the performance and the related features have been rarely considered so far. In this paper, we aim to design a kind of GMS with ferrite materials, termed magnetic

*syliu@zjnu.cn

plasmonic GMSs due to the excitation of magnetic surface-plasmon (MSP) resonance [52]. Different from the GMSs made of dielectric or metallic materials, the magnetic plasmonic GMSs possess nonreciprocity in virtue of the time-reversal-symmetry-breaking nature of ferrite materials under a bias magnetic field, further enhanced by the MSP resonance [53]. The nonreciprocal GH shift has been observed, which is shown to be tuned either intrinsically by the gradient of the GMSs or extrinsically by the bias magnetic field. In addition, the GH shift is shown to be reversed by reversing the direction of the bias magnetic field, which is basically accomplished by switching between positive and negative angular momentum channels of the ferrite rods [54]. The physical mechanism of the enhanced GH shift and the nonreciprocal behavior can be clearly identified by examining the photonic dispersion curves. Although the present paper is just a proof-of-concept demonstration, the idea can be extended to design nonreciprocal metasurfaces with more exquisite configurations so that the novel physics and potential applications can be expected.

II. NONRECIPROCAL GH SHIFT AT NORMAL INCIDENCE

To be specific, the magnetic plasmonic GMS is composed of an array of ferrite rod dimers with a rotational gradient introduced in the unit cell as illustrated in the insets of Fig. 1. The single-crystal yttrium iron garnet is used for ferrite rods due to the extremely low loss. The electric permittivity of the ferrite rods is $\varepsilon_s = 15 + i3 \times 10^{-3}$, and the magnetic permeability of the fully magnetized ferrite rods along rod axes, namely, the z direction, is given by [55]

$$\widehat{\mu} = \begin{pmatrix} \mu_r & -i\mu_\kappa & 0 \\ i\mu_\kappa & \mu_r & 0 \\ 0 & 0 & 1 \end{pmatrix}, \tag{1}$$

with

$$u_r = 1 + \frac{\omega_m(\omega_0 - i\alpha\omega)}{(\omega_0 - i\alpha\omega)^2 - \omega^2}, \quad u_\kappa = \frac{\omega_m\omega}{(\omega_0 - i\alpha\omega)^2 - \omega^2}, \tag{2}$$

where $\omega_m = 2\pi f_m = 2\pi\gamma M_s$ is the characteristic frequency with the gyromagnetic ratio $\gamma = 2.8$ MHz/Oe, M_s is the saturation magnetization, and $\omega_0 = 2\pi f_0 = 2\pi\gamma H_0$ is the spin-wave resonance frequency with H_0 as the sum of the bias magnetic field applied along the z direction and the demagnetization field. For single-crystal yttrium iron garnet, the saturation magnetization is $M_s = 1750$ G, and the damping coefficient is $\alpha = 3 \times 10^{-4}$, corresponding to the negligible loss. In this case, the magnetic property only reacts to the TM wave mode with the electric field polarized along the rod axes. As a result, the two-dimensional TM Gaussian beam is used to examine the GH shift, except otherwise stated, the beam-waist radius is $w_0 = 3\lambda$ with λ as the operating wavelength. Based on the Mie theory [56] and multiple-scattering theory [57,58], we can simulate the reflection of a Gaussian beam from the metasurfaces, meanwhile, the photonic dispersion curves of the metasurfaces can be retrieved to discover the underlying physics.

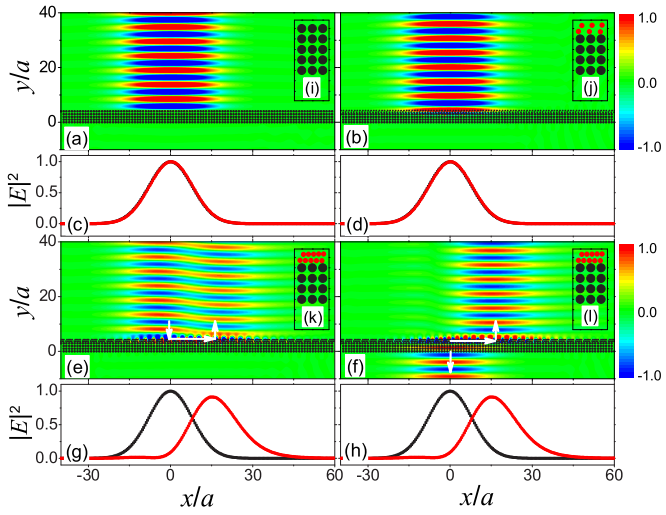

FIG. 1. The electric-field patterns for a transverse magnetic (TM) Gaussian beam incident normally on the surface of a five-layer slab composed of an array of ferrite rods in (a) the square lattice and the situation for the upmost layer of the slab replaced by a magnetic plasmonic GMS with the unit cell containing (b) three and (e) and (f) five pairs of rod dimers. The field intensity profiles for the incident (black line) and reflected (red line) Gaussian beam are shown in (c), (d), and (g), corresponding to (a), (b), and (e), respectively. Panel (f) shows only the scattering field for (e) so that the reflected beam can be clearly observed. Panel (h) is the same as (g), given for the convenience of comparison. Panels (i)–(k) are the unit cells for the corresponding slabs, among which panels (k) and (l) are the same. The operating frequency is 4.76 GHz, and the bias magnetic field is applied such that $H_0 = 500$ Oe.

As a paradigm, we first consider an ordinary periodic surface of a five-layer slab consisting of an array of ferrite rods arranged as a square lattice in the air. The lattice separation is $a = 12$ mm, the rod radius is $r = 5$ mm, and the bias magnetic field is applied such that $H_0 = 500$ Oe. The total reflection of a normally incident Gaussian beam is observed as shown in Fig. 1(a), and there appears no lateral shift along the surface as illustrated in Fig. 1(c) from the complete overlap of field intensity profiles for the incident and reflected beams. The scenario is similar to the case of a dielectric or metallic surface for the normal incident Gaussian beam. Then, we examine the performance for the upmost layer replaced by the GMSs with the unit cell consisting of an array of rod dimers. The size of the unit cell is $a_0 = 3a = 36$ mm, the interparticle separation of the rod dimer is $d = 8$ mm with a rod radius of $r_0 = 2.5$ mm, and an appropriate rotational gradient is introduced in the unit cell. In this case, the rest of the four-layer slab beneath is served as the substrate. For the unit cell containing three pairs of equally separated rod dimers with the rotational angle uniformly varying from 60° to 75°, the configuration is shown in the inset (j). There is still no GH shift as illustrated in Figs. 1(b) and 1(d). Differently, for the unit cell containing five pairs of rod dimers with the same range of rotational angle as shown in the inset (k), an evident rightward shift of the reflected Gaussian beam close to three wavelengths can be observed as demonstrated in Figs. 1(e) and 1(g). From the field profile, we can find explicitly the excitation of the surface wave, coincident with the mechanism in other systems [19]. For convenience, we show in Fig. 1(f)

solely the scattering field so that the reflected beam can be clearly discerned. The unidirectional lateral shift comes from the time-reversal-symmetry breaking of the magnetic system under the bias magnetic field, and the magnetic GMS serves as a platform to couple the incident Gaussian beam to the surface wave. Therefore, this typical unidirectional lateral shift is termed the nonreciprocal GH shift.

III. PHOTONIC DISPERSION CURVES AND GH AT OBLIQUE INCIDENCE

To gain a deeper understanding of the phenomenon, we calculate the photonic dispersion curves as shown in Fig. 2 where a PBG can be observed for the magnetic metamaterials due to the MSP resonance [52] indicated by a dense set of flat bands so that the Gaussian beam can be totally reflected as shown in Fig. 1. Then, we also calculate the dispersion curves of edge modes for different interfaces as plotted in Figs. 2(b) and 2(c) to illustrate the different GH shifts shown in Fig. 1. For the five-layer slab considered in Fig. 1(a), the dispersion curves are two symmetric branches inside the PBG as marked by the black squares. But they actually lie outside the light cone since the periodicity along the Γ-X direction is a, not $3a$, resulting in the band folding. The usage of the unit cell in Fig. 1(i) is just for the convenience of comparison. As a result, the incident Gaussian beam cannot be coupled to the edge mode so that no GH shift can be achieved, explaining the *in situ* total reflection of the Gaussian beam in Fig. 1(a). For the five-layer slab in Fig. 1(b) with the unit cell in Fig. 1(j), the dispersion curves are denoted by the blue triangles in Fig. 2(b). Although they lie inside the light cone, there still appears no coupling of the incident Gaussian beam with the edge mode due to the small density of states and the mismatch of the parallel component of the wave vector, corresponding to the zero GH shift in Figs. 1(b) and 1(d). For the unit cells with different rotational angles, the dispersion curves are also shown in Fig. 2(b), and they exhibit similar styles, showing that the edge mode of the GMS with this configuration is not easy to tune, and the GMS is inappropriate for realizing the GH shift. Differently, for the unit cell containing five pairs of rod dimers in Fig. 1(k) the dispersion curves are shown in Fig. 2(c) and denoted by the blue triangles where the high density of states and the match of the parallel component of the wave vector at the working frequency of 4.76 GHz for normal incidence ensure the strong coupling of the incident Gaussian beam with the edge modes as shown in Figs. 1(e) and 1(f), resulting in the evident GH shift. Besides, by tuning the range of rotational angle in the unit cells, the dispersion curves can be flexibly controlled, adding additional degrees of freedom in manipulating the GH shift.

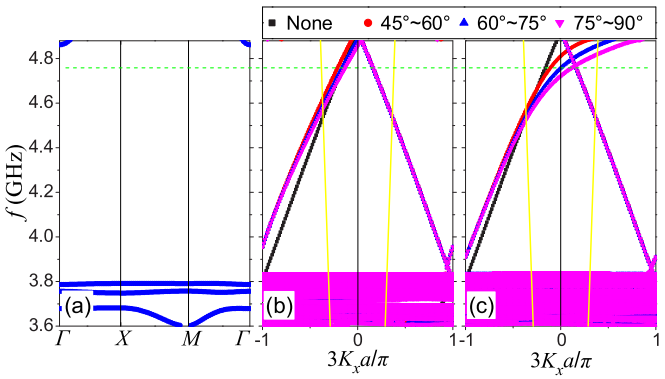

FIG. 2. (a) The photonic dispersion curves for the bulk magnetic metamaterial of the square lattice, showing a photonic band gap (PBG) on the top of the flat bands. (b) The photonic dispersion curves of edge modes along the Γ-X direction for the five-layer slab cutting out from the magnetic metamaterial with the unit cell shown in Fig. 1(i) (black squares) and that with the upmost layer replaced by the GMS, whose unit cell contains three pairs of rod dimers with the rotational angle θ uniformly varying from 45° to 60° (red circles), from 60° to 75° as typically shown in Fig. 1(j) (blue triangles), and from 75° to 90° (magenta triangles). Panel (c) is the same as panel (b) except that the unit cell contains five pairs of rod dimers with the rotational angle varying in the same range. The unit cell with the rotational angle ranging from 60° to 75° is typically shown in Fig. 1(k). The green dashed line marks the working frequency at 4.76 GHz in Figs. 1 and 3, and the solid yellow lines mark the light lines. The other parameters are the same as those in Fig. 1.

From the photonic dispersion curves in Fig. 2(c), it can be found that the magnetic GMS with different rotational gradients couples to the edge modes at different directions. For the unit cell with the rotational angle ranging from 60° to 75°, the normal incidence corresponds to the strongest coupling and leads to the largest GH shift. When the rotational angle in the unit cell is decreased to a smaller range from 45° to 60°, the oblique incidence with $k_{\|} < 0$ (the Gaussian beam incident from the right-hand side at the incident angle $\theta_{\text{inc}} = -6°$) corresponds to the best coupling and exhibits an evident GH shift according to the match of the parallel wave vector for the incident beam and the edge mode in Fig. 2(c). The associated scattering field pattern is shown in Fig. 3(a) where we can find a notable rightward lateral shift, although the reflected Gaussian beam is deformed a little bit. Differently, for the Gaussian beam incident from the left-hand side at a geometrically symmetric angle $\theta_{\text{inc}} = 6°$, only a tiny lateral shift is demonstrated as shown in Fig. 3(b) due to the mismatch of the Gaussian beam with the edge mode as can also be discerned from the field intensity profile shown in Fig. 3(d). On the contrary, for the magnetic GMS with the rotational angle in the unit cell increased to the range from 75° to 90°, the rightward lateral shift is relatively larger for the Gaussian beam incident from the left-hand side with the incident angle $\theta_{\text{inc}} = 4°$ as shown in Figs. 3(e) and 3(g), which coincides with the associated photonic dispersion curve in Fig. 2(c) where $k_{\|} > 0$ is required to achieve a better coupling. As a result, the GH shift is smaller for the Gaussian beam incident from the right-hand side with the incident angle $\theta_{\text{inc}} = -4°$, but the rightward lateral shift is still evident. The situation is distinct from that shown in Figs. 3(a) and 3(b) due to the relatively smaller oblique incident angle, which can be explained detailedly in the next section. It should be noted that for all the cases the rightward GH shift is observed, which is determined by the orientation of the bias magnetic field. By reversing the bias magnetic field from the z to the $-z$ direction, the GH shift will be reversed to be the leftward lateral shift.

As pointed out in the pioneering work by Yu's Group, the abrupt phase change at each scatter in the unit cell of

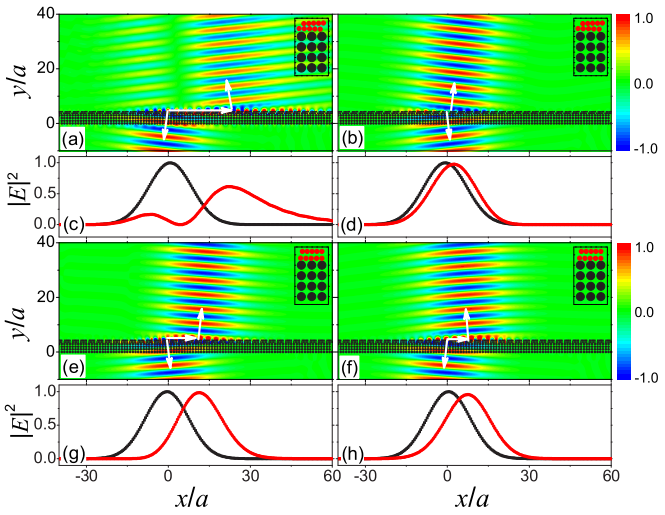

FIG. 3. Nonreciprocal GH shift for a TM Gaussian beam incident obliquely on a five-layer slab with the upmost layer a magnetic GMS of the rotational angle from 45° to 60° (a) and (b) and 75° to 90° (e) and (f). The oblique incident angles corresponding to panels (a), (b), (e), and (f) are $-6°$, $6°$, $4°$, and $-4°$, respectively. The field intensity profiles close to the interface for the incident (black line) and reflected (red line) Gaussian beam are shown in (c), (d), (g), and (h), corresponding to (a), (b), (e), and (f), respectively. The working frequency is 4.76 GHz, and the other parameters are the same as those in Fig. 1.

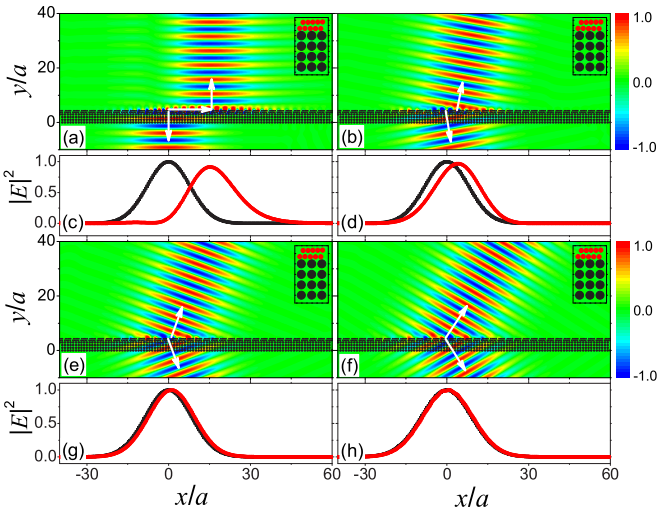

FIG. 4. The electric-field patterns for a TM Gaussian beam incident on a five-layer slab with the upmost layer a magnetic GMS of the rotational angle from 60° to 75° at the incident angle (a) $\theta_{inc} = 0°$, (b) $\theta_{inc} = 10°$, (e) $\theta_{inc} = 20°$, and (f) $\theta_{inc} = 30°$, respectively. The field intensity profiles close to the interface for the incident (black line) and reflected (red line) Gaussian beams are shown in (c), (d), (g), and (h), corresponding to (a), (b), (e), and (f), respectively. Panels (a) and (c) are the same as Figs. 1(f) and 1(h), given here for the convenience of comparison.

metasurface can give rise to an effective momentum vector, resulting in anomalous reflection and refraction [36]. Differently, from the electric-field patterns shown in Figs. 1 and 3, it is clear that the incident angle is equal to the angle of reflection, indicating that there is no effective momentum vector compensating the wave vector of the reflection beam from the magnetic GMS. The purpose of our paper is to manipulate the GH shift, and we thus try to avoid the occurrence of anomalous reflection. Actually, the anomalous reflection can be achieved by constructing the magnetic GMS with an appropriate rotational gradient. The magnetic GMS in the present paper is served to tailor the surface mode so that the coupling strength can be controlled, offering a degree of freedom to manipulate the GH shift. Although we cannot obtain the exact formula to give the direct connection between the GH shift and the coupling strength to the surface wave, in several historical literatures [19,20,59,60] the enhancement of the GH shift was implemented by exciting the surface waves. To illustrate the similar effect in our paper qualitatively, we have simulated the field patterns for the Gaussian beam incident on the magnetic GMS at different angles as shown in Fig. 4 where we can find that the largest GH shift appears at normal incidence as shown in panels (a) and (c), corresponding to the strongest coupling as indicated from the photonic band diagram in Fig. 2(c). The GH shift decreases evidently with increasing the incident angle to be $\theta_{inc} = 10°$ as shown in panels (b) and (d). When the incident angle is increased to be $\theta_{inc} = 20°$ or 30°, corresponding to even weaker coupling, nearly no evident GH shift can be discerned by examining panels (e)–(h). Therefore, the weaker the incident photons couple to the surface wave, the smaller the GH shift is. In principle, by engineering the magnetic GMS the coupling strength can be flexibly controlled, and thus the GH shift can be tuned.

IV. TUNABILITY BY THE ROTATIONAL GRADIENT AND THE BIAS MAGNETIC FIELD

From the aforementioned results, it can be found that the GH shift is strongly dependent on the rotational gradient of the magnetic GMS as illustrated from both the photonic dispersion curves and the electric-field patterns. To present an even clearer picture, we have calculated the GH shift as the function of the incident angles θ_{inc} for the magnetic GMSs with different rotational gradients. The results are shown in Fig. 5(a) where the solid black line in panel (a) shows the corresponding result for the magnetic GMS concerned in Figs. 3(a) and 3(b). The abrupt change in the GH shift indicates that it is strongly dependent on the incident angle, resulting in the remarkable difference for the geometrically symmetric incidence, in good agreement with the field pattern analysis. The peak value of the GH shift is about $25a$, close to 5λ. In addition, for the whole range of the incident angles, the GH shift is positive (namely, rightward lateral shift), signifying a nonreciprocal feature of the GH shift in the system. Then, we turn to the magnetic GMS considered in Figs. 1(e) and 1(f), and the corresponding result is denoted by the red solid line, showing the largest GH shift about 3λ for the normal incidence, inconsistent with the photonic dispersion curves shown in Fig. 2(c). For the magnetic GMSs inspected in Figs. 3(e) and 3(f), the result is depicted by the blue solid lines where only a slow variation of the GH shift is exhibited with respect to the incident angle. Therefore, the

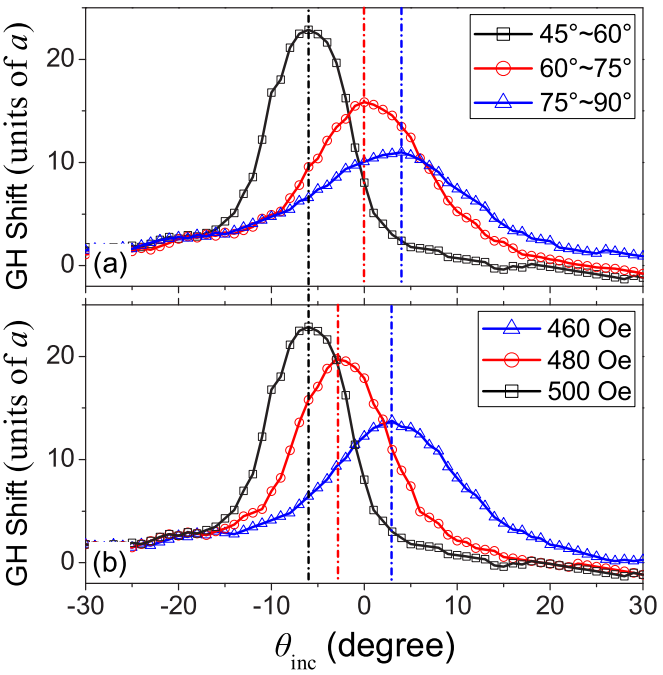

FIG. 5. (a) The GH shift is plotted as the function of incident angle $\theta_{\rm inc}$ for three different magnetic GMSs with the rotational angles ranging from 45° to 60°, from 60° to 75°, and from 75° to 90°, respectively, under a bias magnetic-field $H_0 = 500$ Oe. (b) For a fixed magnetic GMS with the rotational angle ranging from 45° to 60°, the GH shift is plotted as the function of incident angle $\theta_{\rm inc}$ under three different bias magnetic fields such that H_0 is equal to 460, 480, and 500 Oe, respectively. The working frequency is 4.76 GHz, and the other parameters are the same as those in Fig. 1.

difference in the GH shift is not evident in Figs. 3(e) and 3(f) compared to that shown in Figs. 3(a) and 3(b). Actually, it is known that the reflection phase Φ at the interface between two homogeneous media is a function of the incident angle $\theta_{\rm inc}$. As a result, the GH shift can be calculated analytically according to Artmann's formula [7],

$$D = -\frac{1}{k}\frac{d\Phi}{d\theta_{\rm inc}}, \tag{3}$$

where k is the wave number in the background medium. Differently, the magnetic GMS in our paper is an inhomogeneous interface, and thus the reflection phase cannot be obtained analytically. However, based on Eq. (3) and the simulation results shown in Fig. 5, we can arrive at a very interesting conclusion that the reflection phase Φ exhibits the most significant variation with respect to the incident angle $\theta_{\rm inc}$ when the strongest coupling of the incident photons with the magnetic GMS is triggered. As a consequence, the tunability of the GH shift by the magnetic GMS can be interpreted as the manipulation of the reflection phase by controlling the rotational gradient. By examining Fig. 5 once again, we can find that a relatively larger GH shift will emerge at the peak when the curve is more sensitive to the incident angle, in agreement with the above analysis to some extent.

By tuning the configuration of the magnetic GMS, we intrinsically change the morphology of the GMS. It can be used to control the electromagnetic properties of the magnetic GMS, offering the tunability on the GH effect. However, it is not convenient in experiment or in exploring possible applications. To implement the controllability with more degrees of freedom, the extrinsic manipulation is preferred. Concretely, for a specific magnetic GMS with the rotational angle ranging from 45° to 60°, we can tune the bias magnetic field so that the electromagnetic properties can be freely adjusted. As the typical examples, the GH shift under three different bias magnetic fields are shown in Fig. 5(b) where the peak value of the GH shift can be flexibly tuned, similar to the intrinsic control in panel (a). For both the intrinsic and the extrinsic cases, we note that the incident angle associated with the peak value is changed from negative to positive. To be specific, in panel (b), by tuning H_0 from 460 to 480 Oe, the incident angle at the peak is altered from 3° to −3°. This transition can be clearly demonstrated by examining the photonic dispersion curves, similar to that shown in Fig. 2(c) where the parallel component of the wave vector is altered from $k_\parallel > 0$ to $k_\parallel < 0$ at the operating frequency when the rotational angle is transformed. However, we should point out that for the magnetic GMS considered in present paper the controllable range of incident angle is still not large enough. Fortunately, the GH shift for the normal incidence with $\theta_{\rm inc} = 0$ already has a notable magnitude, which cannot be observed in a nonmagnetic system. Moreover, the GH shift can be switched to the opposite direction by reversing the magnetization, offering an additional degree of freedom.

To present an even clearer illustration how the nonreciprocal GH shift is controlled by the bias magnetic field, we have simulated the scattering electric-field patterns at the optimal incident angle and under three different bias magnetic fields [corresponding to three peaks shown in Fig. 5(b)]. The results are shown in Fig. 6 where the rightward GH shift does not exhibit evident difference for the incident angles $\theta_{\rm inc} = \pm 3°$ under $H_0 = 460$ and 480 Oe as shown in panels (a)–(d). This arises from the weak angular dependence of the GH shift, in agreement with the slowly varying curves in Fig. 5(b). However, we can still observe that the relatively larger GH shift is switched from the left-hand side incidence with $\theta_{\rm inc} = 3°$ in panel (a) to the right-hand side incidence with $\theta_{\rm inc} = -3°$ in panel (c). This transition indicates that the edge mode can be modulated by the bias magnetic field so that the optimal coupling angle is changed. When the bias magnetic field is increased to $H_0 = 500$ Oe, the angular dependence becomes significant around the peak as indicated by the black solid line in Fig. 5(b), in good agreement with the remarkably different behaviors shown in Figs. 6(e) and 6(f). The field patterns in Figs. 6(e) and 6(f) are actually the same as Figs. 3(a) and 3(b), given here just for the convenience of comparison. It is emphasized that by reversing the bias magnetic field from the z to the $-z$ direction the GH shift is reversed to the opposite direction as clearly demonstrated in Figs. 6(g) and 6(h), which originates from the nonreciprocity of the magnetic system. In particular, the reversion manipulation also works for both oblique and normal incidences, making the switching effect flexibly controlled. It should be noted that the magnetic GMS can also be operated as a coupler to convert the incident wave into the surface mode and simultaneously control the phase, reminiscent of the earlier work by Sun and co-workers [50]. Differently, in our case the incident wave will be coupled

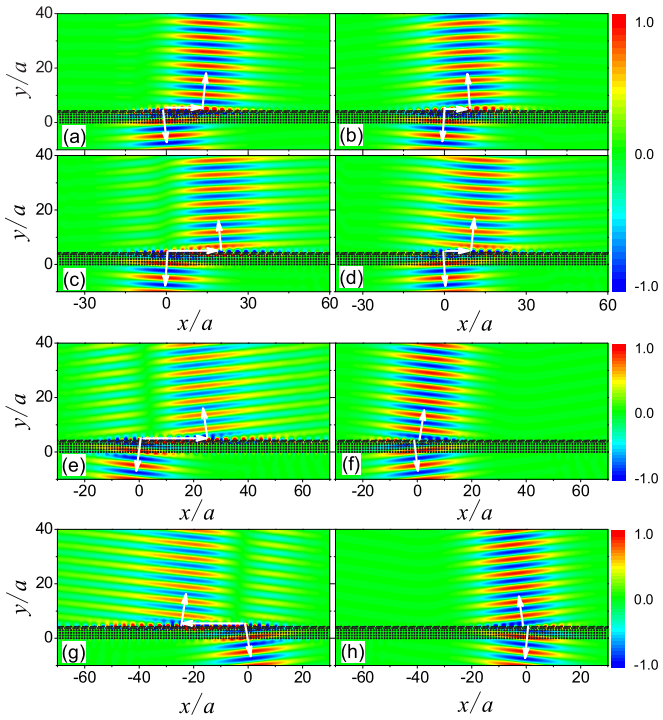

FIG. 6. Manipulating the nonreciprocal GH shift extrinsically by tuning the bias magnetic field so that $H_0 = 460$ Oe for (a) and (b), $H_0 = 480$ Oe for (c) and (d), and $H_0 = 500$ Oe for panels (e)–(h). The incident angles are 3° for (a) and (d), −3° for (b) and (c), −6° for (e) and (h), and 6° for (f) and (g), respectively. The magnetic GMS has the rotational angle ranging from 45° to 60°, the same as Fig. 5(b), the working frequency is 4.76 GHz, and the other parameters are the same as those in Fig. 1.

unidirectionally due to the time-reversal-symmetry-breaking nature of the magnetic GMS under a bias magnetic field. Following the concept in the present paper, we can expect even more nonreciprocal functionalities implemented by magnetic GMS.

V. CONCLUSIONS

In conclusion, we have designed a kind of magnetic plasmonic GMSs composed of an array of ferrite rods with a rotation gradient introduced to the rod dimers in the unit cell. It can be operated as a platform to implement nonreciprocal GH shift, which can be controlled intrinsically by tuning the rotational gradient or extrinsically by tuning the bias magnetic field for a specified magnetic GMS. The physical mechanism can be discovered by examining the dispersion curve of the edge mode where a single branch of the dispersion curve signifies the nonreciprocal characteristic of the magnetic GMS and the variation of dispersion curve with respect to the rotational gradient and the bias magnetic field explains the angular dependence of the phenomenon. In particular, the extrinsic manipulation with a bias magnetic field can flexibly control the optimal incident angle, the operating frequency, as well as the unidirectionality of the GH shift. The proof-of-concept demonstration of the nonreciprocal GH effect supported by the magnetic GMS can serve as a guide for experimental verification and potential applications.

ACKNOWLEDGMENTS

This work was supported by the Zhejiang Provincial Natural Science Foundation of China (Grant No. LR16A040001), the National Natural Science Foundation of China (Grants No. 11574275, No. 11747025, and No. 61464001), the open project of the State Key Laboratory of Surface Physics in Fudan University (Grant No. KF2017_4), the Research Program of Science for Universities of Guang Xi Autonomous Region (Optical properties of metamaterials with disordered and gradient surfaces and the design of electromagnetic devices), and the Scientific Research Starting Foundation of Guangxi University of Science and Technology (Grant No. 16z03).

[1] F. Goos and H. Hänchen, Ann. Phys. (NY) **436**, 333 (1947).
[2] F. I. Fedorov, Dokl. Akad. Nauk. SSR **105**, 465 (1955).
[3] C. Imbert, Phys. Rev. D **5**, 787 (1972).
[4] O. de Beauregard and C. Imbert, Phys. Rev. D **7**, 3555 (1973).
[5] I. V. Shadrivov, R. W. Ziolkowski, A. A. Zharov, and Y. S. Kivshar, Opt. Express **13**, 481 (2005).
[6] J. B. Götte, W. Löffler, and M. R. Dennis, Phys. Rev. Lett. **112**, 233901 (2014).
[7] K. Artmann, Ann. Phys. (NY) **437**, 87 (1948).
[8] R. H. Renard, J. Opt. Soc. Am. **54**, 1190 (1964).
[9] W. J. Wild and C. L. Giles, Phys. Rev. A **25**, 2099 (1982).
[10] L. G. Wang, H. Chen, and S. Y. Zhu, Opt. Lett. **30**, 2936 (2005).
[11] M. Merano, A. Aiello, G. W. 't Hooft, M. P. van Exter, E. R. Eliel, and J. P. Woerdman, Opt. Express **15**, 15928 (2007).
[12] V. J. Yallapragada, A. V. Gopal, and G. S. Agarwal, Opt. Express **21**, 10878 (2013).
[13] O. Emile, T. Galstyan, A. Le Floch, and F. Bretenaker, Phys. Rev. Lett. **75**, 1511 (1995).
[14] D. L. Gao and L. Gao, Appl. Phys. Lett. **97**, 041903 (2010).
[15] J. C. Martinez and M. B. A. Jalil, Europhys. Lett. **96**, 27008 (2011).
[16] S. Z. Chen, C. Q. Mi, L. Cai, M. X. Liu, H. L. Luo, and S. C. Wen, Appl. Phys. Lett. **110**, 031105 (2017).
[17] X. Yin and L. Hesselink, Appl. Phys. Lett. **89**, 261108 (2006).
[18] M. Merano, A. Aiello, M. P. van Exter, and J. P. Woerdman, Nat. Photonics **3**, 337 (2009).
[19] D. Felbacq and R. Smaâli, Phys. Rev. Lett. **92**, 193902 (2004).
[20] I. V. Soboleva, V. V. Moskalenko, and A. A. Fedyanin, Phys. Rev. Lett. **108**, 123901 (2012).
[21] X. Chen, L. G. Wang, and C. F. Li, Phys. Rev. A **80**, 043839 (2009).
[22] Y. D. Xu, C. T. Chan, and H. Y. Chen, Sci. Rep. **5**, 8681 (2015).
[23] A. Namdar, I. V. Shadrivov, and Y. S. Kivshar, Phys. Rev. A **75**, 053812 (2007).
[24] J. S. Wu, D. N. Basov, and M. M. Fogler, Phys. Rev. B **92**, 205430 (2015).
[25] L. Lambrechts, V. Ginis, J. Danckaert, and P. Tassin, Phys. Rev. B **95**, 035427 (2017).

[26] R. Briers, O. Leroy, and G. Shkerdin, J. Acoust. Soc. Am. **108**, 1622 (2000).
[27] V.-O. de Haan, J. Plomp, T. M. Rekveldt, W. H. Kraan, A. A. van Well, R. M. Dalgliesh, and S. Langridge, Phys. Rev. Lett. **104**, 010401 (2010).
[28] X. Chen, C. F. Li, and Y. Ban, Phys. Rev. B **77**, 073307 (2008).
[29] P. Gruszecki, M. Mailyan, O. Gorobets, and M. Krawczyk, Phys. Rev. B **95**, 014421 (2017).
[30] C. W. J. Beenakker, R. A. Sepkhanov, A. R. Akhmerov, and J. Tworzydło, Phys. Rev. Lett. **102**, 146804 (2009).
[31] Q. D. Jiang, H. Jiang, H. W. Liu, Q. F. Sun, and X. C. Xie, Phys. Rev. Lett. **115**, 156602 (2015).
[32] A. V. Kildishev, A. Boltasseva, and V. M. Shalaev, Science **339**, 1232009 (2013).
[33] N. F. Yu and F. Capasso, Nature Mater. **13**, 139 (2014).
[34] B. Walther, C. Helgert, C. Rockstuhl, F. Setzpfandt, F. Eilenberger, B. Kley, F. Lederer, A. Tünnermann, and T. Pertsch, Adv. Mater. **24**, 6300 (2012).
[35] Y. B. Xie, W. Q. Wang, H. Y. Chen, A. Konneker, B. I. Popa, and S. A. Cummer, Nat. Commun. **5**, 5553 (2014).
[36] N. F. Yu, P. Genevet, M. A. Kats, F. Aieta, J. P. Tetienne, F. Capasso, and Z. Gaburro, Science **334**, 333 (2011).
[37] X. J. Ni, N. K. Emani, A. V. Kildishev, A. Boltasseva, and V. M. Shalaev, Science **335**, 427 (2012).
[38] J. P. Balthasar Mueller, N. A. Rubin, R. C. Devlin, B. Groever, and F. Capasso, Phys. Rev. Lett. **118**, 113901 (2017).
[39] Z. Y. Li, M. H. Kim, C. Wang, Z. H. Han, S. Shrestha, A. C. Overvig, M. Lu, A. Stein, A. M. Agarwal, M. Lončar, and N. F. Yu, Nat. Nanotechnol. **12**, 675 (2017).
[40] X. B. Yin, Z. L. Ye, J. Rho, Y. Wang, and X. Zhang, Science **339**, 1405 (2013).
[41] W. J. Luo, S. L. Sun, H. X. Xu, Q. He, and L. Zhou, Phys. Rev. Appl. **7**, 044033 (2017).
[42] N. F. Yu, F. Aieta, P. Genevet, M. A. Kats, Z. Gaburro, and F. Capasso, Nano Lett. **12**, 6328 (2012).
[43] A. Pors and S. I. Bozhevolnyi, Opt. Express **21**, 2942 (2013).
[44] M. Khorasaninejad, Z. Shi, A. Y. Zhu, W. T. Chen, V. Sanjeev, A. Zaidi, and F. Capasso, Nano Lett. **17**, 1819 (2017).
[45] O. Avayu, E. Almeida, Y. Prior, and T. Ellenbogen, Nat. Commun. **8**, 14992 (2017).
[46] G. X. Zheng, H. Mühlenbernd, M. Kenney, G. X. Li, T. Zentgraf, and S. Zhang, Nat. Nanotechnol. **10**, 308 (2015).
[47] W. W. Wan, J. Gao, and X. D. Yang, Adv. Opt. Mater. **5**, 1700541 (2017).
[48] X. H. Zhang, J. J. Jin, M. B. Pu, X. L. Li, X. L. Ma, P. Gao, Z. Y. Zhao, Y. Q. Wang, C. T. Wang, and X. G. Luo, Nanoscale **9**, 1409 (2017).
[49] X. Y. Duan, S. Kamin, and N. Liu, Nat. Commun. **8**, 14606 (2017).
[50] S. L. Sun, Q. He, S. Y. Xiao, Q. Xu, X. Li, and L. Zhou, Nature Mater. **11**, 426 (2012).
[51] O. Y. Yermakov, A. I. Ovcharenko, A. A. Bogdanov, I. V. Iorsh, K. Y. Bliokh, and Y. S. Kivshar, Phys. Rev. B **94**, 075446 (2016).
[52] S. Y. Liu, J. J. Du, Z. F. Lin, R. X. Wu, and S. T. Chui, Phys. Rev. B **78**, 155101 (2008).
[53] S. Y. Liu, W. L. Lu, Z. F. Lin, and S. T. Chui, Appl. Phys. Lett. **97**, 201113 (2010).
[54] S. Y. Liu, W. L. Lu, Z. F. Lin, and S. T. Chui, Phys. Rev. B **84**, 045425 (2011).
[55] D. M. Pozar, *Microwave Engineering*, 4rd ed. (Wiley, New York, 2012).
[56] W. H. Eggimann, IRE Trans. Microwave Theory Tech. **8**, 440 (1960).
[57] D. Felbacq, G. Tayeb, and D. Maystre, J. Opt. Soc. Am. A **11**, 2526 (1994).
[58] S. Y. Liu and Z. F. Lin, Phys. Rev. E **73**, 066609 (2006).
[59] I. V. Shadrivov, A. A. Zharov, and Y. S. Kivshar, Appl. Phys. Lett. **83**, 2713 (2003).
[60] T. Paul, C. Rockstuhl, C. Menzel, and F. Lederer, Phys. Rev. A **77**, 053802 (2008).